

An Empirical Study on the Performance of Wireless OFDM Communications in Highly Reverberant Environments

Ryan Measel*, Christopher S. Lester*, Donald J. Bucci*, Kevin Wanuga*
Gregory Tait†, Richard Primerano*, Kapil R. Dandekar*, Moshe Kam*

*Department of Electrical and Computer Engineering
Drexel University, Philadelphia, PA 19104

†Electromagnetic & Sensor Systems Department
Naval Surface Warfare Center, Dahlgren, VA 22448

Abstract—Reverberation chambers are closed, reflective spaces that can emulate highly reverberant electromagnetic environments. The electromagnetic environment is primarily determined by the size of the cavity, effective conductivity, and leakage via apertures. In this effort, we investigate the performance of wireless OFDM communications in relation to the latter two by controlling the loading of a reverberation chamber and the effective aperture into a coupled cavity. A software defined radio measurement platform was used to assess the communication performance through a selection of link-level metrics including error vector magnitude, post processing signal-to-noise ratio, and throughput. The degradation of link quality is quantified for increasingly diffuse environments, as well as the improvement when leveraging a maximal ratio combining receiver diversity scheme. The link quality was found to improve in both the reverberation chamber and the coupled cavity for larger effective apertures. This result was analyzed using a time-dependent model for RF propagation in coupled cavities.

I. INTRODUCTION

Interest exists around deploying wireless networks in confined, reflective spaces that are electromagnetically coupled, such as those found in the naval, aviation, automotive, and warehouse industries [1]–[5]. In particular, below-deck spaces in naval vessels have been a primary focus of a number of studies in recent years which explored both RF propagation [6]–[12] and wireless communication performance [13]–[16].

Highly reverberant environments are characterized by rich electromagnetic scattering resulting in multipath interference for wireless communications. Reflective surfaces cause multiple copies of the transmitted signal to arrive at the receiver with variations in time, amplitude, and phase. The combination of these signals can cause fading and distortion which degrades the link quality [17]. The time-depression characteristics of a wireless channel are often characterized through the RMS delay spread. Typical indoor environments (e.g., residential and office) exhibit RMS delay spreads in the range of 15–100 ns at 2.4 GHz [18] whereas highly reverberant environments can reach up to 1200 ns [19]. The objective of this work is to investigate the performance of wireless Orthogonal Frequency-Division Multiplexing (OFDM) communications in such highly reverberant environments.

A. Related Work

Reverberation chambers are rich isotropic multipath environments, suitable for over-the-air testing of small antennas [20], [21]. Reverberation chambers have been used in previous wireless studies on topics including antenna diversity gain [22], throughput modeling [23], and Multiple-Input Multiple-Output (MIMO) OFDM performance [24], [25]. Wireless channel emulation using reverberation chambers was also addressed in [26]–[31]. In this effort, a reverberation chamber is used to experimentally evaluate the performance of wireless OFDM communications by emulating highly diffuse wireless channels.

The electromagnetic environment of a reflective cavity is heavily influenced by the size of the cavity, effective conductivity, and leakage via apertures [10]. The effective conductivity and aperture leakage are controllable properties and the primary experimental parameters evaluated in this work.

The effective conductivity is controlled by loading the reverberation chamber with electromagnetic absorbing foam. In [32], requirements were presented for effective loading based on the physical parameters of the reverberation chamber. Several works have demonstrated how loading can be used to control the characteristics of the wireless channel including the Rician K-factor [33] and the power delay profile [29]. Control of the power delay profile enables emulation of diffuse wireless channels, such as those found in office, industrial [30], and outdoor urban environments [34]. Similarly, in this work, a range of highly diffuse channels are emulated by varying the loading.

The effective aperture of a reflective cavity is a combination of all electromagnetic leakage from seals, seams, joints, and gaps (e.g., doors, windows). Leakage between closed cavities forms a coupled system. A number of RF propagation studies and modeling efforts have focused on coupled systems [19], [35]–[38]. A time-dependent model was developed in [19], [35] that can estimate wireless channel parameters based on RF propagation measurements.

A special phenomenon, known as the “keyhole effect,” is

related to coupled cavities and has been the subject of recent interest. First proposed in [39], the keyhole effect occurs when MIMO capacity is low (comparable to single-input single-output) despite uncorrelated channels. The keyhole effect was observed experimentally in [40], [41]. It is not applicable to this work as the slot aperture between the coupled cavities is not analogous to a keyhole aperture. Furthermore, in a previous study [19], it was experimentally proven that the cavities under test in this work exhibit Rayleigh fading even when weakly coupled, unlike the double fading channel that results from the keyhole effect.

B. Experiment Description

We experimented across a series of configurations for the loading of the reverberation chamber and the coupling between the reverberation chamber and a coupled cavity. Coupling was controlled by varying the size of the slot aperture adjoining the cavities. The configured electromagnetic environments were characterized through impulse response measurements. The parameters of the resulting wireless channels were estimated using the time-dependent model from [19], [35].

We evaluated the wireless performance through link-level metrics including error vector magnitude, post-processing signal-to-noise ratio, and achievable throughput. Wireless OFDM measurements were obtained at 2.4 GHz (analogous to the IEEE 802.11 [42]) using a software defined radio platform [43]. Additionally, the maximal ratio combining receiver diversity scheme is evaluated. The performance metrics and experimental parameters were selected specifically for their relevance to design and implementation of wireless networks (e.g., wireless LANs and remote sensor systems) in shipboard environments.

The remainder of the paper is organized as follows. Section II discusses how the wireless environment of the reverberation chamber was configured to emulate highly reverberant environments. The experimental setup, including the test protocol and performance metrics, is described in Section III. The results are presented in Section IV and summarized in Section V.

II. ENVIRONMENT CONFIGURATION

A. Environment Description

Experiments were performed in a reverberation chamber provided by the Naval Surface Warfare Center Dahlgren Division at the Naval Support Facility Dahlgren. The reverberation chamber (Volume 1) has a volume of 97 m³. A coupled cavity (Volume 2) is adjoined via a 1 m × 2 m shielded door and has a volume of 34 m³. The environment is stirred by two mechanical Z-fold tuners (2.7 meter in length) that are located in the Volume 1. Figure 1 shows a cross section of the reverberation chamber along with the connecting doorway, mechanical tuners, and wireless node placements.

B. Electromagnetic characterization

The electric field of a reflective space can be altered by mechanical stirring, frequency stirring, loading, etc. Deterministic analysis through measurement or simulation can

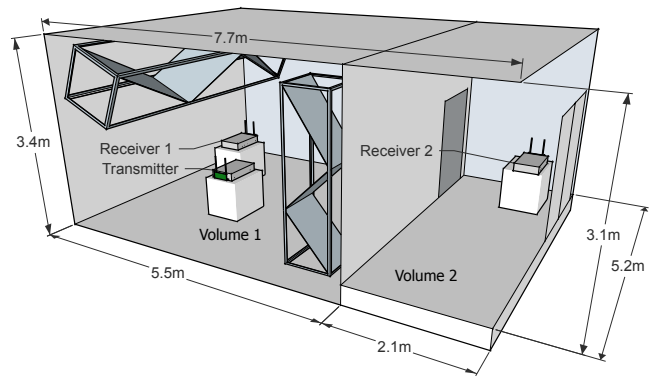


Fig. 1. Cross section of the reverberation chamber. Two mechanical Z-fold tuners are used to stir the environment. The Transmitter and Receiver 1 were positioned in the Volume 1 (with LOS), while Receiver 2 was positioned behind the door in Volume 2 (without LOS).

not adequately characterize the nature of such environments, necessitating the use of stochastic methods. A time-domain measurement approach is presented in [10] that estimates the exponential energy decay time (τ) based on the slope of the average received power curve (m , dB/ μ s) as

$$\tau = -\frac{4.34\text{dB}}{m}. \quad (1)$$

This approach is independent of antenna efficiency, which is beneficial as rigorous testing is required to appropriately measure antenna efficiency in a reverberation chamber [44].

Additional parameters that characterize the RF propagation environment of a cavity can be estimated using τ such as the cavity quality factor (Q) and average mode bandwidth. The quality factor Q provides a quantifiable measure of the resonant modes of an excited cavity [45]. It is defined as

$$Q = \frac{f}{\Delta f} \quad (2)$$

where f is the resonant frequency and Δf the half-power bandwidth. It relates to τ via

$$Q = \omega\tau \quad (3)$$

where ω is the angular resonant frequency. The energy loss rate coefficient is

$$\Lambda \equiv \frac{wV}{Q} \quad (4)$$

where V is the volume of the cavity.

The average mode bandwidth,

$$\Delta f = \frac{f}{Q}, \quad (5)$$

is an alternative to Q for expressing the average power transfer function in a reverberation chamber [46]. It can be used to determine the approximate number of excited modes in the reverberation chamber.

C. Time-dependent model for coupled cavities

In a coupled system, the leakage between cavities impacts the energy loss rate. A time-dependent model for coupled cavities was developed in [19], [35] that describes the energy loss for a generalized number of coupled cavities. In the 2-cavity case, a closed form solution exists for the wireless channel parameters of mean delay and RMS delay spread. The solution is based on the eigenvalue energy delay time constants, τ_α and τ_β ,

$$\tau_\alpha \equiv -\frac{1}{\alpha} \quad (6)$$

$$\tau_\beta \equiv -\frac{1}{\beta} \quad (7)$$

$$\alpha = \frac{-\gamma + \sqrt{\gamma^2 - 4\kappa^2}}{2} \quad (8)$$

$$\beta = \frac{-\gamma - \sqrt{\gamma^2 - 4\kappa^2}}{2} \quad (9)$$

$$\gamma = \frac{\Lambda_2 + \Lambda_{2,1}}{V_2} + \frac{\Lambda_1 + \Lambda_{2,1}}{V_1} \quad (10)$$

$$\kappa^2 = \frac{\Lambda_1\Lambda_2 + \Lambda_1\Lambda_{2,1} + \Lambda_2\Lambda_{2,1}}{V_1V_2} \quad (11)$$

$$\Lambda_{i,j} \equiv \frac{1}{2}c\langle\sigma_{i,j}\rangle \quad (12)$$

$$i \neq j \quad (14)$$

where Λ_i is the energy loss rate coefficient in Volume i . $\Lambda_{i,j}$ is the energy loss rate coefficient due to coupling from Volume i to Volume j . V_i is the volume of Volume i . c is the speed of light. $\sigma_{i,j}$ is the effective aperture cross section, and the angled brackets $\langle \rangle$ represents averaging over a 2π -steradian solid angle of wave incidence [35].

1) *Mean Delay*: The mean delay is the average delay of all multipath components reaching the receiver and is defined as the first-order moment of the Power Delay Profile (PDP) [47]. Using the time-dependent model [19], the mean delay, τ_0 , is calculated from the eigenvalue energy delay time constants,

$$\tau_0 = \tau_\alpha + \tau_\beta. \quad (15)$$

2) *RMS Delay Spread*: The RMS delay spread, τ_{RMS} , is a measure of the richness of the scattering environment and is defined as the second-order moment of the PDP [47]. Using the time dependent model [19], the RMS delay spread, τ_{RMS} , is calculated from the eigenvalue energy delay time constants,

$$\tau_{\text{RMS}} = \sqrt{\tau_\alpha^2 + \tau_\beta^2}. \quad (16)$$

3) *Coherence Bandwidth*: The coherence bandwidth, B_c , is the range of frequencies over which a channel is correlated. It can be defined in several ways, though it is always inversely proportional to the RMS delay spread. In this work, the coherence bandwidth will be considered the half-power bandwidth at which the complex autocorrelation function has a value larger than 0.5. The coherence bandwidth under this definition [46] is

$$B_c = \frac{1}{\frac{2\pi}{\sqrt{3}}\sigma_\tau}. \quad (17)$$

TABLE I
EFFECTIVE TRANSMISSION CROSS SECTION ($\langle\sigma_{2,1}\rangle$) AND COUPLING ENERGY LOSS RATE COEFFICIENT ($\Lambda_{2,1}$) FOR THE EFFECTIVE APERTURES OF THE COUPLING CONFIGURATIONS.

Parameter	Coupling		
	Weak	Medium	Strong
$\langle\sigma_{2,1}\rangle$ (m ²)	0.95	0.38	0.90
$\Lambda_{2,1}$ (m ³ /s)	1.43×10^7	5.70×10^7	1.35×10^8

It was further shown in [46] that the coherence bandwidth is proportional to the average mode bandwidth in a loaded reverberation chamber.

D. Effective Transmission Coefficient

The effective transmission cross section is required to calculate the energy loss rate coefficient of coupling between the cavities as per Equation 6. According to the geometric optics approximation in [45], the effective transmission cross section can be approximated using the surface area (A) of the aperture [35],

$$\langle\sigma_{i,j}\rangle \cong A/2. \quad (18)$$

Three (3) configurations were selected where the door was mostly closed (Weak Coupling), partially open (Medium Coupling), and mostly open (Strong Coupling). The values of the effective transmission cross sections and the coupling energy loss rate coefficients for the configurations are shown in Table I.

E. Measurement Protocol

The measurement protocol is the same as described in [10]. The channel transfer function was measured over the forward transmission coefficient, S_{21} , between two antennas attached to a network analyzer. Two dual-ridged, horn antennas were used as the transmitter and receiver. The antennas were positioned away from the cavity boundaries and each other at an oblique angle. The antennas were cross polarized. A 200 MHz, 1601-point frequency sweep was performed with a dwell time of 5 ms, intermediate frequency bandwidth of 50 kHz, and a center frequency of 2.462 GHz (IEEE 802.11, Channel 11 [48]). Each measurement was averaged over 25 independent positions of the stirrers. The impulse response was found by taking the inverse discrete Fourier transform of the channel transfer function. The impulse response of the wireless channel was calculated as the ensemble average of 20 time-resolved measurements.

F. Loading Configurations

Volume 1 (reverberation chamber) was loaded with electromagnetic absorbing foam blocks, measuring 60 cm by 60 cm by 15 cm. Three (3) configurations were selected that have RMS delay spreads of 444 ns, 529 ns, and 1045 ns and Q factors of 5954 (High Q), 3014 (Medium Q), and 2537 (Low Q), respectively. At 2.462 GHz, the cavity quality factor Q of the unloaded cavity is approximately 14,000. To

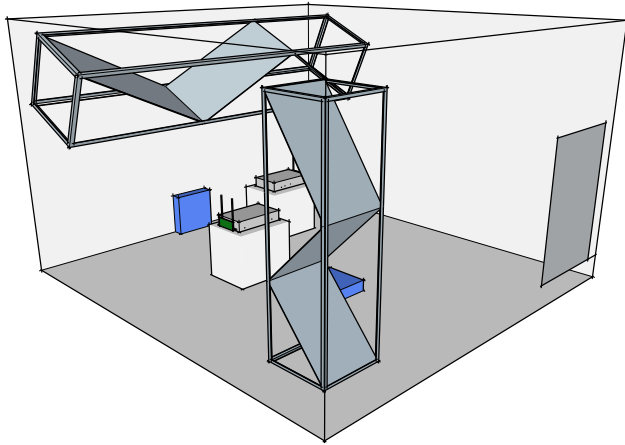


Fig. 2. Isometric view of the reverberation chamber with the positions of the 2 absorbers for the High Q configuration.

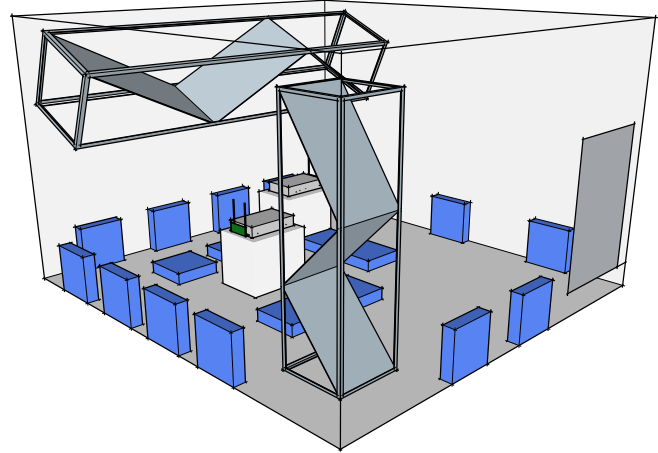


Fig. 4. Isometric view of the reverberation chamber with the positions of the 19 absorbers for the Low Q configuration.

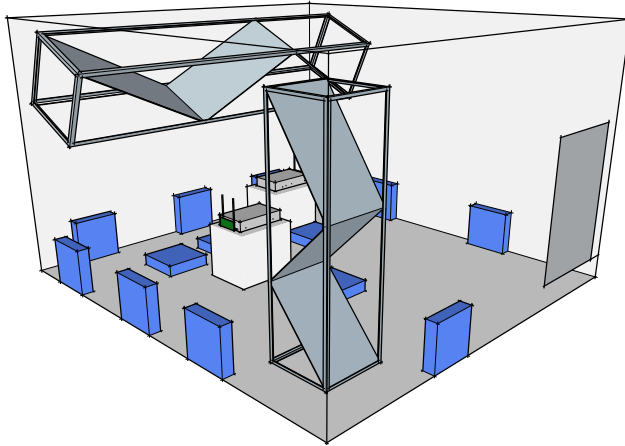


Fig. 3. Isometric view of the reverberation chamber with the positions of the 13 absorbers for the Medium Q configuration.

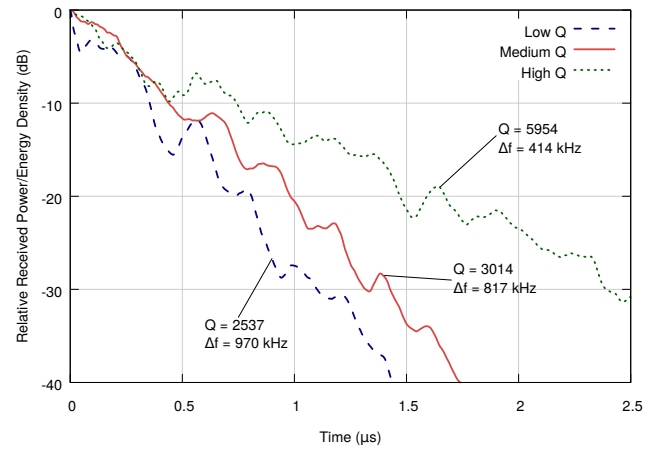


Fig. 5. Impulse responses of Volume 1 across the loading configurations. Q and Δf are estimated from the slope of the response. Increasing the loading causes energy in the chamber to dissipate at a faster rate resulting in a lower Q .

create these configurations, 2, 13, and 19 foam blocks were used for High Q (Figure 2), Medium Q (Figure 3), and Low Q (Figure 4), respectively. The impulse responses of Volume 1 across the configurations are shown in Figure 5. The corresponding electromagnetic environment parameters are presented in Table II. The wireless channel parameters calculated empirically from the PDP are presented in Table III.

Volume 2 (coupled cavity) was unloaded for all testing. The impulse response is shown in Figure 6, and the electromagnetic

environment parameters are shown in Table IV. For all loading configurations, the coupling between the chambers was held constant at the Coupling 2 configuration. The wireless channel parameters estimated using the time-dependent model for coupled cavities (Section II-C) are shown in Table V.

G. Coupling Configurations

The impulse responses for Volume 1 across the coupling configurations are shown in Figure 7. The electromagnetic

TABLE II
ELECTROMAGNETIC ENVIRONMENT PARAMETERS FOR VOLUME 1 AT 2.462 GHz FOR THE LOADING CONFIGURATIONS.

Parameter	Q		
	Low	Medium	High
τ (ns)	164	195	385
Q	2537	3014	5954
Δf (kHz)	970	817	414
Λ_1 (m ³ /s)	5.85×10^8	4.93×10^8	2.49×10^8

TABLE III
WIRELESS CHANNEL PARAMETERS FOR VOLUME 1 AT 2.462 GHz FOR THE LOADING CONFIGURATIONS.

Parameter	Q		
	Low	Medium	High
Mean Delay (ns)	1257	1497	2957
RMS Delay Spread (ns)	444	529	1045
Coherence Bandwidth (kHz)	620	521	264

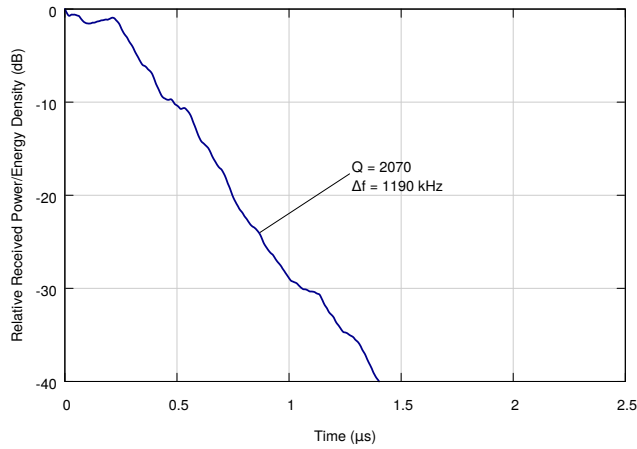


Fig. 6. Impulse response of Volume 2. Q and Δf are estimated from the slope of the response. Volume 2 was unloaded across all loading and coupling configurations.

TABLE IV
ELECTROMAGNETIC PARAMETERS FOR VOLUME 2 AT 2.462 GHz.

Parameter	Volume 2
τ (ns)	134
Q	2070
Δf (kHz)	1190
Λ_2 (m ³ /s)	2.55×10^8

parameters for Volume 1 are presented in Table VI. The effect of coupling on the energy decay in Volume 1 is not as pronounced as the effect of loading. For stronger coupling, more energy leaks into the coupled cavity which increases the loss rate in Volume 1. The wireless channel parameters are presented in Table VII. The RMS delay spread decreases for stronger coupling, which implies link quality improves in Volume 1 as the coupling increases.

The wireless channel parameters for Volume 2 are presented

TABLE V
WIRELESS CHANNEL PARAMETERS FOR VOLUME 2 AT 2.462 GHz FOR THE LOADING CONFIGURATIONS.

Parameter	Q		
	Low	Medium	High
Mean Delay (ns)	263	289	437
RMS Delay Spread (ns)	190	212	347
Coherence Bandwidth (kHz)	1454	1302	794

TABLE VI
ELECTROMAGNETIC ENVIRONMENT PARAMETERS FOR VOLUME 1 AT 2.462 GHz FOR THE COUPLING CONFIGURATIONS.

Parameter	Coupling		
	Weak	Medium	Strong
τ (ns)	208	195	162
Q	3223	3014	2502
Δf (kHz)	764	816	984
Λ_1 (m ³ /s)	4.61×10^8	4.93×10^8	5.94×10^8

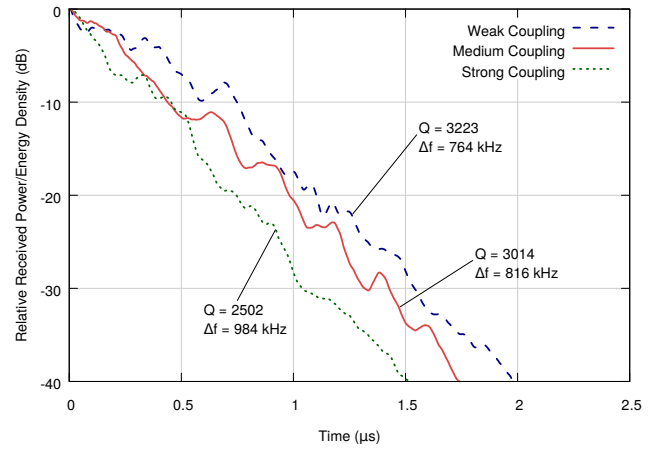


Fig. 7. Impulse responses of Volume 1 across the coupling configurations. Q and Δf are estimated from the slope of the response. Energy dissipates from Volume 1 at a faster rate when the chambers are strongly coupled.

TABLE VII
WIRELESS CHANNEL PARAMETERS FOR VOLUME 1 AT 2.462 GHz FOR THE COUPLING CONFIGURATIONS.

Parameter	Coupling		
	Weak	Medium	Strong
Mean Delay (ns)	1603	1497	1243
RMS Delay Spread (ns)	597	529	440
Coherence Bandwidth (kHz)	486	521	627

in Table VIII. The values are calculated using the time-dependent energy model in Section II-C. Similarly to Volume 1, the RMS delay spread decreases for stronger coupling, which implies link quality improves as coupling increases.

III. EXPERIMENTAL SETUP

A. Measurement Platform

A MATLAB-based, Software-Defined Radio (SDR) measurement platform [43] was used in conjunction with the Wireless Open Access Research Platform (WARP), an SDR FPGA platform built by Rice University [49]. Two physical layer schemes were implemented using the WARPlab-interface: Single-Input Single-Output (SISO) and Maximal Radio Combining (MRC).

The Orthogonal Frequency-Division Multiplexing (OFDM) frames were fashioned after the IEEE 802.11g protocol [48] with a bandwidth of 10 MHz subdivided across 64 subcarriers (156.26 kHz per subcarrier), of which 48 carried data using

TABLE VIII
WIRELESS CHANNEL PARAMETERS FOR VOLUME 2 AT 2.462 GHz FOR THE COUPLING CONFIGURATIONS.

Parameter	Coupling		
	Weak	Medium	Strong
Mean Delay (ns)	316	289	260
RMS Delay Spread (ns)	228	212	196
Coherence Bandwidth (kHz)	1208	1302	1404

Binary Phase Shift Keying (BPSK). Each packet contained 20 OFDM words for a total of 960 data symbols. Transmission occurred at a center frequency of 2.462 GHz (IEEE 802.11, Channel 11 [48]).

All nodes were outfitted with dual-band (2.4/5.8 GHz) omnidirectional antennas (L-com, model HG2458RD-SM). The Transmitter had a single antenna while the receivers had two.

B. Node Deployment

Three (3) nodes were used in the experiments, one (1) transmitter and two (2) receivers. The Transmitter and Receiver 1 were deployed in Volume 2. Receiver 1 had Line-Of-Sight (LOS) to the Transmitter, thereby experiencing Rician fading. Receiver 2 was deployed in Volume 2 behind the shielded door such that it did not have LOS into Volume 1, thereby experiencing Rayleigh fading [47]. The node locations are shown in Figure 1. Due to the isotropic nature of a reverberation chamber, the positioning of the nodes is not significant as long as they are sufficiently far from cavity boundaries and the stirrers. All nodes were elevated off the ground by non-absorbing Styrofoam blocks.

C. Experiment Protocol

At the start of each experiment, the transmit gain was calibrated using an Agilent U2001H USB Power sensor to ensure equal gains across all tests. An experiment consisted of 500 transmissions where each transmission contained 960 symbols for a total of 480,000 samples per experiment. The channel was tuned every 10 transmissions by rotating the two Z-fold mechanical tuners. No stirring occurred during transmissions to ensure analogous channels across varying experimental parameters.

D. Wireless Performance Metrics

1) *Error Vector Magnitude*: Error Vector Magnitude (EVM) is the magnitude of the vector between a transmitted symbol and the received symbol. The distribution of the EVM is used to assess the quality of communications and has been shown to be a reliable predictor of signal integrity at the physical layer [50].

2) *Post-Processing Signal-to-Noise Ratio*: Post-Processing Signal-to-Noise Ratio (PP-SNR) is defined as the ratio of signal power to signal error [50],

$$\text{PP-SNR} = \mathbb{E} \left[\frac{\|x\|^2}{\|\hat{x} - x\|^2} \right] \approx \frac{1}{\text{EVM}^2}. \quad (19)$$

In addition to channel noise, PP-SNR includes noise resulting from the specific hardware and processing implementation (e.g., non-linear distortion in the radio transceiver, error in channel estimation, and noise enhancement from equalization) [14].

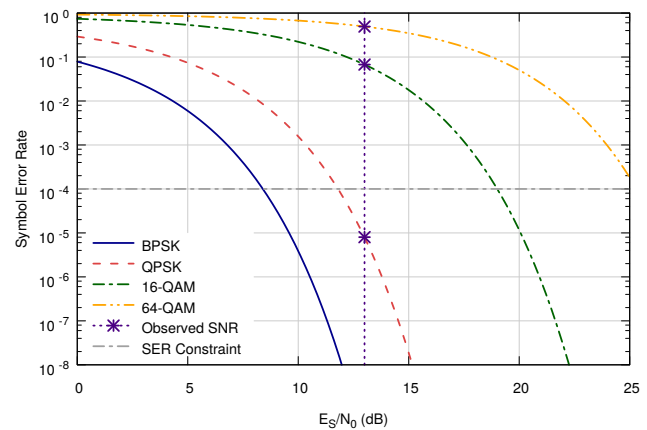


Fig. 8. The theoretical symbol error rate curves for common, base-2 modulation schemes are shown [47]. Modulation schemes which fall below the selected SER constraint at observed PP-SNR are supported. In this example, both BPSK and QPSK can operate under the SER constraint of 10^{-4} at a SNR of 13 dB.

3) *Achievable Throughput*: Throughput is the amount of data successfully transmitted to a receiver per unit time (bps). The measurement platform implements the packet structure of IEEE 802.11g, but it does not implement inter-packet timing and collision avoidance. Individual packet transmissions are triggered by the platform after the receive buffers of the SDR have been downloaded over the Ethernet backchannel. Since the number of packets sent per unit time is not analogous to IEEE 802.11g, it is not possible to directly measure the link throughput.

The achievable throughput can be estimated using the observed SNR and a Symbol Error Rate (SER) constraint [50]. The theoretical SER for a modulation scheme can be determined from the SNR [47]. Conversely, when the SER is constrained, the minimum SNR needed to achieve that constraint can be determined. Thus, when the SNR of a link is measured, the supported modulation schemes can be determined by specifying an SER constraint. Any modulation scheme which has a SER below the constraint at the observed SNR will be supported.

Determining supported schemes for a measured SNR is demonstrated in Figure 8. The theoretical SER curves are plotted for BPSK (Eq. 6.6 [47]), Quadrature Phase Shift Keying (QPSK) (Eq. 6.7 [47]), 16 Quadrature Amplitude Modulation (QAM), and 64-QAM (Eq. 6.23 [47]). A vertical line is extended at the observed SNR of a link (13 dB). A horizontal line is extended at the selected SER constraint (10^{-4}). A modulation scheme is supported at that SNR if its curve intersects the vertical SNR threshold below the SER constraint. Both BPSK and QPSK intersect the SNR threshold at SERs below the constraint, so they are supported with an achievable throughput of 6 and 12 Mbps, respectively. It is also possible to use this process to estimate the SER for a specified modulation scheme. Using the same observed SNR of 13 dB, the link would incur an SER of 3.4×10^{-2} if the 16-QAM modulation scheme was used.

The throughput (T) can be estimated using the modulation

order (M , number of symbols in the constellation) and the symbol rate (S , Baud per second) [51],

$$T = S \log_2 M. \quad (20)$$

The symbol rate of an OFDM word is calculated as

$$S = B \frac{N_{DSC}}{N_{SC}}, \quad (21)$$

where B is the bandwidth, N_{SC} is number of subcarriers, and N_{DSC} is number of data subcarriers.

In this measurement platform, the frames are constructed with 64 subcarriers (including 48 data subcarriers) and a 16 sample cyclic extension. Therefore, the symbol rate is

$$S = 10\text{MHz} \frac{48}{64 + 16} = 6\text{MBdps}. \quad (22)$$

No coding schemes are considered, so the modulation schemes of BPSK, QPSK, 16-QAM, and 64-QAM correspond to achievable throughputs of 6, 12, 18, and 24 Mbps, respectively.

IV. RESULTS

Two physical layer schemes were used by the receivers: Single-Input Single-Output (SISO) and 1×2 Maximal Ratio Combining (MRC) [47]. For SISO, only one of the receive antenna was used.

Note, the Cumulative Distribution Function (CDF) plots of the Error Vector Magnitude (EVM) use decibel values, $10 \log_{10}(\text{EVM})$. This convention is used to ease the comparison of the links at relatively small values ($\ll 0.1$). Since it is desirable for EVM to be as low as possible, better performance is indicated by a distribution that tends towards the upper left of the plot.

Across all configurations, High Q has the smallest coherence bandwidth of 264 kHz (Section II). The wireless measurement platform has a subcarrier bandwidth 156.25 kHz (Section III-A). Since the subcarrier bandwidth is less than the coherence bandwidth, the channel is correlated and exhibits frequency-flat fading [47]. Thus, the performance presented in this section is receiver-noise limited and not subject to intersymbol interference.

A. Loading

Three (3) loading configurations (as described in Section II-F) were tested for both the Line-Of-Sight (LOS) receiver in Volume 1 and the Non-Line-Of-Sight (NLOS) receiver in Volume 2. For all loading configurations, the coupling of Volume 1 was held constant at the Medium Coupling configuration.

1) *LOS Receiver*: The RMS delay spread increased substantially from 444 ns at Low Q to 1045 ns at High Q . Accordingly, the link quality degraded. This trend is exemplified in Figures 9 and 10, which show the CDF of the EVM and the Post-Processing Signal-to-Noise Ratio (PP-SNR) for both SISO and MRC, respectively. Increasing the RMS delay spread shifted the distribution towards a higher median EVM. The PP-SNR for SISO decreased by nearly 11 dB from Low Q to High Q .

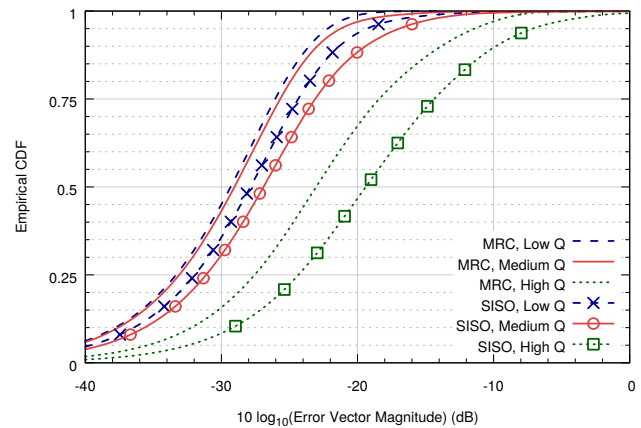


Fig. 9. CDF of the EVM for the LOS receiver across the loading configurations. Higher Q environments (with larger RMS delay spread) produced distributions with higher median EVM. MRC substantially improved over SISO in each configuration.

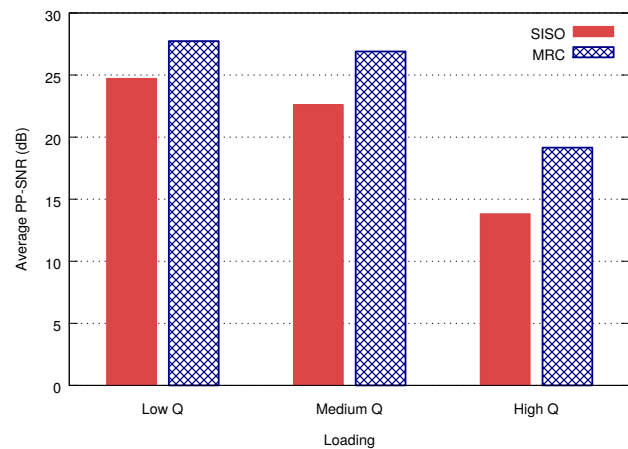


Fig. 10. PP-SNR for the LOS receiver across the loading configurations. The higher error rates of the Medium Q and High Q configurations resulted in decreased PP-SNR. The benefit of MRC over SISO was greater as the RMS delay spread grew larger.

MRC had a notable gain in signal quality over SISO. The PP-SNR of MRC decreased as the RMS delay spread increased, but it decreased less than SISO. The gap between MRC and SISO grows from 3.0 dB at Low Q to 5.3 dB at High Q . MRC computes the weighted average of both received streams, so it was expected to outperform SISO. At a higher RMS delay spread, received streams have lower correlation, thereby receiver diversity is more effective. The mitigation provided by receiver diversity is further shown by the CDFs of the EVM for SISO and MRC at High Q (Figure 9). SISO has a larger median EVM and a heavier tail than MRC.

The throughput for the LOS receiver is shown in Table IX. MRC outperformed SISO by 6 Mbps due to its improved PP-SNR.

2) *NLOS Receiver*: The link quality showed moderate improvement as the scattering increased in Volume 1 (Figures 11 and 12). The largest improvement is between Low Q and Medium Q . As expected, MRC outperformed SISO in all

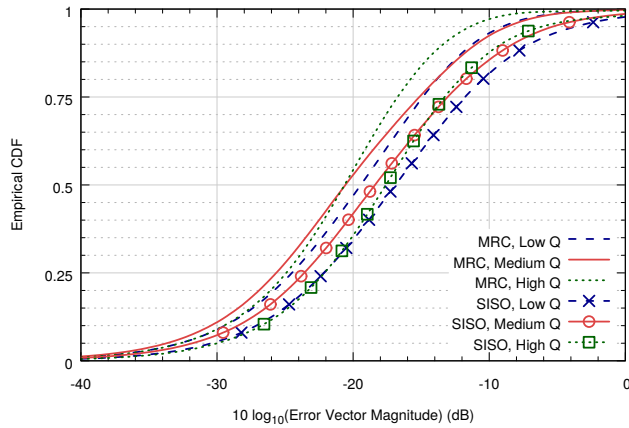


Fig. 11. CDF of the EVM for the NLOS receiver across the loading configurations. For both SISO and MRC, the Low Q and Medium Q distributions had heavier tails than High Q . There is a greater probability of symbols on those links incurring large error.

TABLE IX
ACHIEVABLE THROUGHPUT (Mbps) FOR THE LOS RECEIVER WITH SYMBOL ERROR RATE CONSTRAINED TO 10^{-4} .

Physical Layer Scheme	Q		
	Low	Medium	High
SISO	18	18	12
MRC	24	24	18

configurations. The difference in PP-SNR between SISO and MRC is 4.6 dB at Low Q and 4.7 dB at High Q , so, unlike the LOS case, there is no significant change in the gap.

The throughput for the NLOS receiver with both physical layer schemes is shown in Table X. There is not a significant difference in the throughput of SISO and MRC for the NLOS receiver. MRC only has a higher throughput in the Low Q configuration. Despite the notable gains in PP-SNR for MRC in the Medium Q and High Q configurations, the PP-SNR is still within the same quantized range for the selected Symbol Error Rate (SER), thus the throughput does not increase.

B. Cavity Coupling

The coupling between the cavities was varied across three (3) configurations as described in Section II-D. For all coupling configurations, the loading of Volume 1 was held constant at the Medium Q configuration.

The CDFs of the EVM are shown for the LOS receiver and NLOS receiver in Figures 13 and 14, respectively. The PP-

TABLE X
ACHIEVABLE THROUGHPUT (Mbps) FOR THE NLOS RECEIVER WITH SYMBOL ERROR RATE CONSTRAINED TO 10^{-4} .

Physical Layer Scheme	Q		
	Low	Medium	High
SISO	6	12	12
MRC	12	12	12

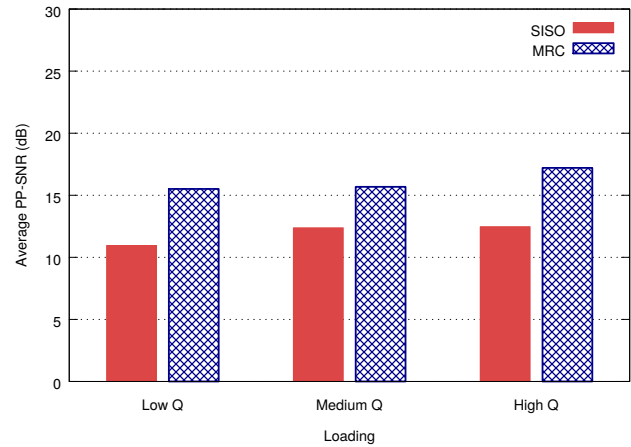


Fig. 12. PP-SNR for the NLOS receiver across the loading configurations. Increasing the scattering in the Volume 1 improved the signal quality in Volume 2.

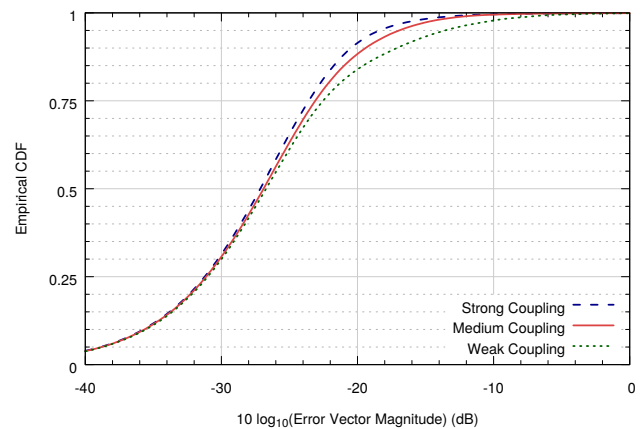


Fig. 13. CDF of the EVM for the LOS receiver across the coupling configurations. Reducing the effective aperture increased the RMS delay spread in the Volume 1 and caused a heavier tail on the EVM distribution.

SNRs of both receivers are shown in Figure 15. Performance improved for both receivers as the effective aperture increased. PP-SNR improved by approximately 3 dB between Weak Coupling and Strong Coupling.

With stronger coupling, more energy leaks via the aperture into Volume 2. The RMS delay spread decreased from 567 ns to 440 ns between Weak Coupling and Strong Coupling (Table VII), thereby the link quality of LOS receiver improves.

The performance improvement of the NLOS link is less in-

TABLE XI
ACHIEVABLE THROUGHPUT (Mbps) FOR THE LOS AND NLOS RECEIVERS ACROSS THE COUPLING CONFIGURATIONS WITH SYMBOL ERROR RATE CONSTRAINED TO 10^{-4} .

Receiver	Coupling		
	Low	Medium	High
LOS	18	18	18
NLOS	6	12	12

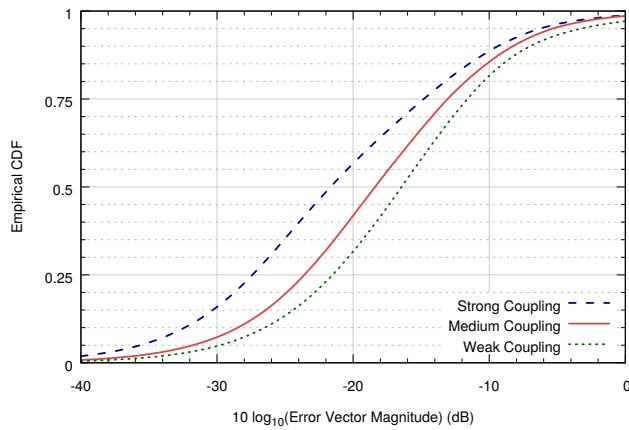


Fig. 14. CDF of the EVM for the NLOS receiver across the coupling configurations. Decreasing the effective aperture resulted in a higher median and a heavier tail.

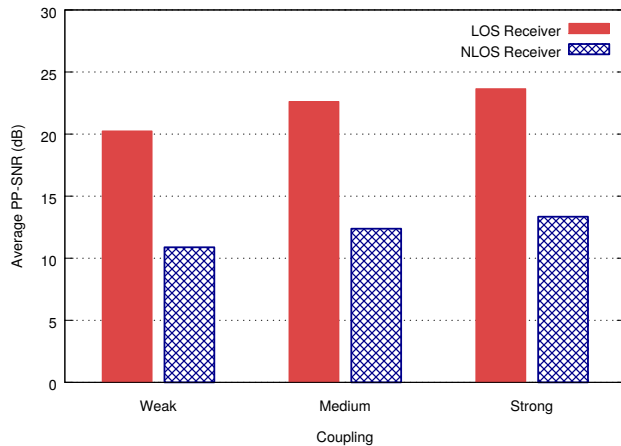


Fig. 15. PP-SNR for the LOS and NLOS receivers across the coupling configurations. The performance improved for both receivers as the effective aperture increased due to the reduction in RMS delay spread.

tuitive. In the coupled cavity model discussed in Section II-C, the net relationship between the effective aperture and the RMS delay spread is inversely proportional. The RMS delay spread decreases from 228 ns to 196 ns from Weak Coupling to Strong Coupling which results in the moderate performance improvement.

The throughput for both receivers across all coupling configurations is shown in Table XI. The improved PP-SNR is not enough to increase the throughput for the LOS receiver, but NLOS increases by 6 dB.

V. CONCLUSION

We studied the performance of wireless OFDM communications in highly reverberant environments through experimentation in a reverberation chamber with a coupled cavity. The loading of the reverberation chamber was controlled to create a range of highly reverberant environments. The electromagnetic properties of the cavities were quantified through time domain impulse measurements. A time-dependent model for RF propagation in coupled cavities was applied in order

to estimate the wireless channel parameters of the coupled system.

Several well known phenomena were validated and quantified through a combination of link-level metrics including error vector magnitude, post processing signal-to-noise ratio, and achievable throughput. Link quality degraded severely for the LOS receiver as the RMS delay spread increased, while the performance of the NLOS receiver in the coupled cavity improved. A receiver diversity scheme was used that substantially improved link performance in both the LOS and NLOS case. The utility of receiver diversity for the LOS case increased with the RMS delay spread.

The impact of cavity coupling was investigated by varying the effective aperture between the connected cavities. The performance of both receivers improved as effective aperture size increased. For the LOS receiver, empirical measurements of the power delay profile show a decrease in RMS delay spread as the effective aperture increases which resulted in the performance improvement. Meanwhile, the coupled cavity model reveals that the RMS delay spread of the wireless channel in a coupled cavity varies inversely to the effective aperture, so the NLOS link quality also improves.

The performance metrics and experimental parameters in this work were selected specifically for their relevance to deployment of wireless networks in shipboard environments. The measurements provided can be used as a baseline for environments in the field with analogous scattering behavior. The EVM and PP-SNR measurements can be used to estimate link quality, while achievable throughput can be used to determine supported modulation schemes and estimate link throughput. The substantial improvements provided by the receiver diversity scheme indicate such a scheme would be well suited for deployment, especially for non-mobile infrastructure (e.g., access points and repeaters) as it places no constraints on the transmitter.

ACKNOWLEDGMENT

The authors thank the members of the Electromagnetic & Sensor Systems Department of the Naval Surface Warfare Center Dahlgren Division for providing access to and assistance with the reverberation chambers.

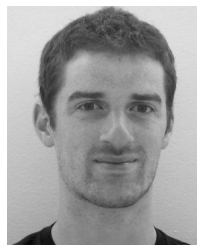
This study was supported by the Office of Naval Research (award N00014-13-1-0312) and also by the National Science Foundation as part of the Wireless Innovation between Finland and United States (WiFiUS) partnership (grant CNS-1147838).

REFERENCES

- [1] V. Gungor and G. Hancke, "Industrial wireless sensor networks: Challenges, design principles, and technical approaches," *IEEE Trans. Ind. Electron.*, vol. 56, no. 10, pp. 4258–4265, Oct 2009.
- [2] P. Angskog, C. Karlsson, J. F. Coll, J. Chilo, and P. Stenumgaard, "Sources of disturbances on wireless communication in industrial and factory environments," in *Proc. Asia-Pacific Symp. on Electromagnetic Compatibility*, 2010.
- [3] G. Tait and P. Opperman, "Electromagnetic compatibility assessment of wireless emissions in shipboard spaces," *In Compliance Magazine*, pp. 28–35, Jun 2013.
- [4] A. Mariscotti, "Experimental determination of the propagation of wireless signals on board a cruise ship," *Measurement*, vol. 44, no. 4, pp. 743–749, 2011.

- [5] A. Sarkar, S. Majumdar, and P. P. Bhattacharya, "Path loss estimation for a wireless sensor network for application in ship," *Int. J. of Comput. Sci. and Mobile Computing*, vol. 2, no. 6, pp. 87–96, 2013.
- [6] M. M. Matthews, "Analysis of radio frequency components for shipboard wireless networks," Master's thesis, Naval Postgraduate School, Dec. 1999.
- [7] D. R. J. Estes, T. B. Welch, A. A. Sarkady, and H. Whitesel, "Shipboard radio frequency propagation measurements for wireless networks," in *Proc. IEEE Military Commun. Conf.*, vol. 1, 2001, pp. 247–251.
- [8] G. Tait and M. Slocum, "Electromagnetic environment characterization of below-deck spaces in ships," in *Proc. IEEE Int. Symp. on Electromagnetic Compatibility*, Aug 2008, pp. 1–6.
- [9] G. Tait, M. Slocum, D. Hilton, C. Dilay, and D. Southworth, "Off-hull radio frequency emissions from below-deck spaces in ships," in *Proc. IEEE Int. Symp. on Electromagnetic Compatibility*, Jul. 2010, pp. 875–880.
- [10] G. Tait, M. Slocum, and R. Richardson, "On multipath propagation in electrically large reflective spaces," *IEEE Antennas Wireless Propag. Lett.*, vol. 8, pp. 232–235, Feb. 2009.
- [11] H. Kdouh, C. Brousseau, G. Zaharia, G. Grunfelder, and G. El Zein, "Measurements and path loss models for shipboard environments at 2.4 GHz," in *Proc. European Microwave Conf.*, Oct. 2011, pp. 408–411.
- [12] G. Tait and C. Hager, "On modeling wireless radio-frequency energy propagation in below-deck ship spaces," in *Proc. IEEE Int. Symp. on Electromagnetic Compatibility*, Aug 2014, pp. 18–23.
- [13] T. Bronez and J. Marshall, "Shipboard experiments for a multihop 802.11 communications system—RF channel characterization and MAC performance measurement," in *Proc. IEEE Military Commun. Conf.*, vol. 1, Oct. 2005, pp. 557–563.
- [14] K. Wanuga, R. Measel, C. S. Lester, D. J. Bucci, D. Gonzalez, R. Primerano, M. Kam, and K. R. Dandekar, "Performance evaluation of MIMO-OFDM systems in on-ship below deck environments," *IEEE Antennas and Wireless Propag. Lett.*, vol. 13, pp. 173–176, January 2014.
- [15] C. S. Lester, R. Measel, D. J. Bucci, K. Wanuga, R. Primerano, M. Kam, and K. Dandekar, "Effects of reconfigurable antennas on wireless network performance within a ticonderoga-class engine room," in *Proc. ASNE Electric Machines Technology Symp.*, May 2014.
- [16] C. S. Lester, D. J. Bucci, R. Measel, K. Wanuga, R. Primerano, K. R. Dandekar, and M. Kam, "Performance of reconfigurable antennas in a below-decks environment," *IEEE Antennas Wireless Propag. Lett.*, vol. 14, pp. 1093–1096, 2015.
- [17] T. Rappaport, *Wireless Communications: Principles and Practice*. Prentice-Hall, 2002.
- [18] V. Erceg *et al.*, "TGN channel models," IEEE, Garden Grove, California, USA, Tech. Rep. P802.11, Jun. 2004.
- [19] G. Tait and R. Richardson, "Wireless channel modeling of multiply connected reverberant spaces: Application to electromagnetic compatibility assessment," *IEEE Trans. Electromagn. Compat.*, vol. 55, no. 6, pp. 1320–1327, Dec 2013.
- [20] P.-S. Kildal and K. Rosengren, "Correlation and capacity of MIMO systems and mutual coupling, radiation efficiency, and diversity gain of their antennas: Simulations and measurements in a reverberation chamber," *IEEE Commun. Mag.*, vol. 42, no. 12, pp. 104–112, Dec 2004.
- [21] P.-S. Kildal, X. Chen, C. Orlenius, M. Franzen, and C. Patane, "Characterization of reverberation chambers for OTA measurements of wireless devices: Physical formulations of channel matrix and new uncertainty formula," *IEEE Trans. Antennas Propag.*, vol. 60, no. 8, pp. 3875–3891, Aug 2012.
- [22] P.-S. Kildal, K. Rosengren, J. Byun, and J. Lee, "Definition of effective diversity gain and how to measure it in a reverberation chamber," *Microwave and Optical Tech. Lett.*, May 2002.
- [23] P.-S. Kildal, A. Hussain, X. Chen, C. Orlenius, A. Skarbratt, J. Asberg, T. Svensson, and T. Eriksson, "Threshold receiver model for throughput of wireless devices with MIMO and frequency diversity measured in reverberation chamber," *IEEE Antennas Wireless Propag. Lett.*, vol. 10, pp. 1201–1204, 2011.
- [24] P.-S. Kildal, C. Orlenius, and J. Carlsson, "OTA testing in multipath of antennas and wireless devices with MIMO and OFDM," *Proc. of the IEEE*, vol. 100, no. 7, pp. 2145–2157, July 2012.
- [25] A. Hussain, P.-S. Kildal, and A. Glazunov, "Interpreting the total isotropic sensitivity and diversity gain of LTE-enabled wireless devices from over-the-air throughput measurements in reverberation chambers," *IEEE Access*, vol. 3, pp. 131–145, 2015.
- [26] A. Pomianek, K. Staniec, and Z. Joskiewicz, "Practical remarks on measurement and simulation methods to emulate the wireless channel in the reverberation chamber," in *Prog. Electromagn. Res.*, vol. 105, 2010, pp. 49–69.
- [27] P.-S. Kildal, "Overview of 6 years R&D on characterizing wireless devices in Rayleigh fading using reverberation chambers," in *Proc. Int. Workshop on Antenna Technology*, March 2007, pp. 162–165.
- [28] J. Frolik, T. Weller, S. DiStasi, and J. Cooper, "A compact reverberation chamber for hyper-Rayleigh channel emulation," *IEEE Trans. Antennas Propag.*, vol. 57, no. 12, pp. 3962–3968, Dec 2009.
- [29] E. Genender, C. Holloway, K. Remley, J. Ladbury, G. Koepke, and H. Garbe, "Use of reverberation chamber to simulate the power delay profile of a wireless environment," in *Proc. Int. Symp. on Electromagnetic Compatibility*, Sept 2008, pp. 1–6.
- [30] —, "Simulating the multipath channel with a reverberation chamber: Application to bit error rate measurements," *IEEE Trans. Electromagn. Compat.*, vol. 52, no. 4, pp. 766–777, Nov 2010.
- [31] C. Holloway, H. Shah, R. Pirkel, K. Remley, D. Hill, and J. Ladbury, "Early time behavior in reverberation chambers and its effect on the relationships between coherence bandwidth, chamber decay time, RMS delay spread, and the chamber buildup time," *IEEE Trans. Electromagn. Compat.*, vol. 54, no. 4, pp. 714–725, Aug 2012.
- [32] C. Holloway, D. Hill, J. Ladbury, and G. Koepke, "Requirements for an effective reverberation chamber: Unloaded or loaded," *IEEE Trans. Electromagn. Compat.*, vol. 48, no. 1, pp. 187–194, Feb 2006.
- [33] C. Holloway, D. Hill, J. Ladbury, P. Wilson, G. Koepke, and J. Coder, "On the use of reverberation chambers to simulate a Rician radio environment for the testing of wireless devices," *IEEE Trans. Antennas Propag.*, vol. 54, no. 11, pp. 3167–3177, Nov 2006.
- [34] H. Fielitz, K. Remley, C. Holloway, Q. Zhang, Q. Wu, and D. Matolak, "Reverberation-chamber test environment for outdoor urban wireless propagation studies," *IEEE Antennas Wireless Propag. Lett.*, vol. 9, pp. 52–56, 2010.
- [35] G. B. Tait, R. E. Richardson, M. B. Slocum, and M. O. Hatfield, "Time-dependent model of RF energy propagation in coupled reverberant cavities," *IEEE Trans. Electromagn. Compat.*, vol. 53, pp. 846–849, 2011.
- [36] J. Giuseppe, C. Hager, and G. Tait, "Wireless RF energy propagation in multiply-connected reverberant spaces," *IEEE Antennas Wireless Propag. Lett.*, vol. 10, pp. 1251–1254, 2011.
- [37] G. Tait, R. Richardson, M. Slocum, M. Hatfield, and M. Rodriguez, "Reverberant microwave propagation in coupled complex cavities," *IEEE Trans. Electromagn. Compat.*, vol. 53, no. 1, pp. 229–232, Feb 2011.
- [38] O. Delangre, P. De Doncker, M. Lienard, and P. Degauque, "Coupled reverberation chambers for emulating MIMO channels," *Comptes Rendus Physique 11*, pp. 30–36, 12 2009.
- [39] D. Chizhik, G. Foschini, M. Gans, and R. Valenzuela, "Keyholes, correlations, and capacities of multielement transmit and receive antennas," *IEEE Trans. Wireless Commun.*, vol. 1, no. 2, pp. 361–368, Apr 2002.
- [40] C. Orlenius and M. Andersson, "Repeatable performance measurements of MIMO systems in connected reverberation chambers with controlled keyhole effect," in *Proc. European Conf. on Antennas and Propagation*, March 2009, pp. 1086–1089.
- [41] P. Almers, F. Tufvesson, and A. Molisch, "Keyhole effect in MIMO wireless channels: Measurements and theory," *IEEE Trans. Wireless Commun.*, vol. 5, no. 12, pp. 3596–3604, December 2006.
- [42] "IEEE standard for information technology—telecommunications and information exchange between systems—local and metropolitan area networks," *IEEE Std 802.11g-2003 (Amendment to IEEE Std 802.11, 1999 Edn. (Reaff 2003) as amended by IEEE Stds 802.11a-1999, 802.11b-1999, 802.11b-1999/Cor 1-2001, and 802.11d-2001)*, pp. i–67, 2003.
- [43] R. Measel, D. J. Bucci, C. S. Lester, K. Wanuga, R. Primerano, K. R. Dandekar, and M. Kam, "A MATLAB platform for characterizing MIMO-OFDM communications with software-defined radios," in *Proc. IEEE Int. Comm. Quality and Rel. Workshop*, May 2014.
- [44] J. Coder, J. Ladbury, and M. Golkowski, "On lower bound antenna efficiency measurements in a reverberation chamber," in *Proc. IEEE Int. Symp. on Electromagnetic Compatibility*, Aug 2012, pp. 216–221.
- [45] D. Hill, M. Ma, A. Ondrejka, B. Riddle, M. Crawford, and R. Johnk, "Aperture excitation of electrically large, lossy cavities," *IEEE Trans. Electromagn. Compat.*, vol. 36, no. 3, pp. 169–178, Aug 1994.
- [46] X. Chen, P.-S. Kildal, C. Orlenius, and J. Carlsson, "Channel sounding of loaded reverberation chamber for over-the-air testing of wireless devices: Coherence bandwidth versus average mode bandwidth and delay spread," *IEEE Antennas Wireless Propag. Lett.*, vol. 8, pp. 678–681, 2009, see also correction in Vol. 12, 2013.

- [47] A. Goldsmith, *Wireless Communications*. New York, NY, USA: Cambridge University Press, 2005.
- [48] *Inform. Technology—Telecommun. and Inform. Exchange Between Syst.—Local and Metropolitan Area Networks—Specific Requirements—Part 11: Wireless LAN Medium Access Control (MAC) and Physical Layer (PHY) Specifications*, IEEE Std. 802.11-1997.
- [49] “WARP Project.” [Online]. Available: <http://warproject.org>
- [50] R. A. Shafik, S. Rahman, R. Islam, and N. S. Ashraf, “On the error vector magnitude as a performance metric and comparative analysis,” in *Proc. Int. Conf. Emerging Technologies*, Nov. 2006, pp. 27–31.
- [51] M. Jankiraman, *Space-time codes and MIMO systems*. Artech House, Inc., 2004.



Ryan Measel (S'07–M'16) received the B.S. degree in Computer Engineering from Drexel University, Philadelphia, Pennsylvania, in 2011. He received the M.S. and Ph.D. degrees in Electrical Engineering also from Drexel University in 2011 and 2015, respectively. At present, he is the Chief Technology Officer of Fantasma Studios. His professional interests include wireless communication, computer vision, mobile applications, autonomous navigation, network protocols, software defined radios, and reconfigurable antennas.



Christopher S. Lester is a Doctoral Candidate in Electrical Engineering at Drexel University. Mr. Lester earned a B.S. and M.S. in Electrical Engineering from Drexel University (2012). His research interests include wireless communication, control systems, robotics and network security.



Donald J. Bucci received the B.S. degree in engineering science from The College of New Jersey in 2009, and the M.S. and Ph.D. degrees in electrical engineering from Drexel University in 2014 and 2015, respectively. Since then, he has been with Lockheed Martin Advanced Technology Laboratories, Cherry Hill, NJ, where he is currently a senior member of the engineering staff. His research interests include data fusion, convex optimization, detection and estimation, wireless communication systems, and signal processing.



Kevin Wanuga (S07) received the B.S. and M.S. degrees in electrical and computer engineering from Drexel University, Philadelphia, PA, USA, where he is currently working toward the Ph.D. degree. His research interests include spectrum sensing, cognitive and adaptive radio algorithms, and microwave techniques.



Gregory Tait is currently an electrical engineer with the Electromagnetic and Sensor Systems Department at the Naval Surface Warfare Center Dahlgren Division in Dahlgren, VA. Previously, he was associate professor of electrical engineering at Virginia Commonwealth University, Richmond, VA, assistant professor of electrical engineering at the United States Military Academy, West Point, NY, and researcher in the Microwave Technology Branch at the Naval Research Laboratory, Washington, DC.

He earned the BA degree in Physics from Amherst College, the MS degree in Electrical Engineering from the University of Maryland, and the PhD degree in Electrical Engineering from The Johns Hopkins University.

Areas of current interest include stochastic electromagnetics in complex cavities, wireless signal propagation, and fiber optic sensors. Dr. Tait has published over 80 papers in peer-reviewed professional journals and conference proceedings.



Richard Primerano received his Ph.D. from Drexel University in 2010. His primary research areas include ultrasonic communication, signal processing, and biologically inspired robotics. His doctoral research focused on the use of ultrasonic signaling to enable high data rate communication through metallic barriers. He has published several peer reviewed works on on-ship RF and ultrasonic communication. More recently, Dr. Primeranos research has focused on ultrasonic power transmission through metal barriers.



Kapil R. Dandekar (S'95–M'01–SM'07) received the B.S. degree in electrical engineering from the University of Virginia in 1997. He received the M.S. and Ph.D. degrees in Electrical and Computer Engineering from the University of Texas at Austin in 1998 and 2001, respectively. In 1992, he worked at the U.S. Naval Observatory and from 1993-1997, he worked at the U.S. Naval Research Laboratory.

In 2001, Dandekar joined the Electrical and Computer Engineering Department at Drexel University in Philadelphia, Pennsylvania. He is currently a Professor in Electrical and Computer Engineering at Drexel University; the Director of the Drexel Wireless Systems Laboratory (DWSL); Associate Dean for Research and Graduate Studies in the Drexel University College of Engineering. DWSL has been supported by the U.S. National Science Foundation, Army CERDEC, National Security Agency, Office of Naval Research, and private industry. Dandekar's current research interests and publications involve wireless, ultrasonic, and optical communications, reconfigurable antennas, and smart textiles. Intellectual property from DWSL has been licensed by external companies for commercialization. Dandekar is also a past member of the IEEE Educational Activities Board and co-founder of the EPICS-in-IEEE program.



Moshe Kam (S'75–M'77–SM'92–F'01) received a B.S. degree in Electrical Engineering from Tel Aviv University in 1976 and M.Sc. and Ph.D. degrees from Drexel University in 1985 and 1987, respectively. He is the Dean of the Newark College of Engineering at the New Jersey Institute of Technology, having served earlier (2007-2014) as the Robert Quinn professor and Department Head of Electrical and Computer Engineering at Drexel University. His professional interests are in system theory, detection and estimation, data fusion, robotics, navigation, and

engineering education. In 2011 he served as President and CEO of IEEE. He had also served member of the Boards of Directors of ABET and the United Engineering Foundation (UEF). He is a Fellow of the IEEE “for contributions to the theory of decision fusion and distributed detection” and recipient of the Eta Kappa Nu C. Holes MacDonald Award (1991) and the IEEE Haraden Pratt Award (2016).